Advances in Basic and Applied Sciences 7 (2025) 1-10

Advances in Basic and Applied Sciences

journal homepage: https://abas.journals.ekb.eg/

Investigating the Relationship Between Plasma Bubbles, Ionospheric Pierce Points, and ROTI Using ASI and GPS Observations.

Nabila Abo-Ahmed [1]*, Amin Fahim Hassan [1], Mohamed Nabil Yasin [1], Mohamed Yousef Omar [1], Ayman Mahrous [1, 2]

[1] *Department of Physics, Faculty of Science, Helwan University, Ain Helwan, Cairo 11792, Egypt*

[2] *Department of Space Environment, Institute of Basic and Applied Sciences, Egypt-Japan University of Science and Technology (E-JUST), New Borg El-Arab City, Alexandria 21934, Egypt.*

ARTICLE INFO

Article history:
Received 11 August 2025
Received in revised form 27 October 2025
Accepted 11 November 2025
Available online 1 December 2025

DOI 10.21608/abas.2025.408255.1076

Keywords: Ionosphere, Airglow, GNSS.

ABSTRACT

This study investigates the plasma bubbles (PBs) over El Leoncito, Argentina, by integrating airglow observations from an all-sky imager (ASI) with ionospheric irregularity signatures derived from the Rate of Total Electron Content Index (ROTI), calculated from GPS measurements, on the night of September 13, 2017. The ASI images captured the full life cycle of multiple PBs, while the GPS observations showed enhanced ROTI values during the time of the bubbles. To enable a direct temporal-spatial correlation between the observed plasma bubble structures, the GPS signal paths, and Roti, the ionospheric pierce points of signals were calculated and projected onto ASI images. The designed projection approach revealed that signals from certain satellites exhibited enhanced ROTI values when their paths passed through airglow depletion regions, confirming that PBs are the source of the observed ionospheric irregularities. This case study provides new evidence that ROTI increases not only during signal passage through the plasma bubbles, but also during transitions from depleted to more uniform ionospheric regions. Such sharp gradients in electron density appear to significantly enhance the ROTI values. In contrast, satellites whose signal paths did not intersect plasma bubbles maintained low and stable ROTI values. This highlights the value of spatial projection techniques in understanding when and where these signal disturbances occur.

1. Introduction

Equatorial plasma bubbles are irregular regions of significantly reduced electron density in the ionosphere, with scale sizes ranging from tens to hundreds of kilometers. These structures primarily originate in the bottomside of the F layer and can extend vertically to higher altitudes.

They typically emerge in equatorial and low-latitude regions, often stretching across the magnetic equator into mid-latitudes [1-3].

---

* **Corresponding author E-mail:** gmnabila431@science.helwan.edu.eg

The development of PBs is closely tied to post-sunset ionospheric dynamics. As solar radiation ceases after sunset, the E region undergoes rapid recombination, leading to a steep vertical gradient in electron density between the depleted E layer and the more persistent F layer.

This gradient creates favorable conditions for the onset of the R-T instability [4]. Simultaneously, the ionospheric dynamo driven by thermospheric winds and reduced E-layer conductivity leads to a prereversal enhancement (PRE) in the eastward electric field, which elevates the F layer through an E×B drift [5]. As the plasma lifted to higher altitudes where the neutral density is low and ion-neutral collisions are less frequent, the growth rate of the R-T instability increases significantly. These combined conditions, strong electron density gradients, elevated F-layer altitudes, and reduced collision frequencies, create an ideal environment for the generation and upward development of Equatorial plasma bubbles [2, 6, 7].

Generally, ionospheric irregularities have a severe impact on the transionospheric propagation of radio waves, causing signal delay and quality degradation. Among these irregularities are PBs, which cause fluctuations in the phase and amplitude of GPS signals, referred to as scintillation, when the signals pass through them. These sometimes result in signal reception failure (loss of lock), increased signal noise, or ultimately positioning errors [8,9]. Therefore, plasma bubbles are widely studied to mitigate and avoid the adverse challenges associated with communication and navigation systems. Different techniques were used in studying plasma bubbles, such as ionosonde observations [10-12], coherent and incoherent scatter radar measurements [13-16], and in situ measurements by Low-Earth Orbiting (LEO) satellites [17-19]. Among the key techniques used in various studies is the ASI, a ground-based optical instrument that captures wide-field airglow emissions, as employed in [20-23]. ASI observations reveal spatial and temporal monitoring of PBs, providing valuable insights into their structure and evolution. On the other hand, GPS measurements are used to compute the ROTI index, which quantifies ionospheric irregularities at various scale sizes [24-26]. It is highly sensitive to the variation in total electron content (TEC) over a short time interval and is widely regarded as an indicator of ionospheric scintillations. Integrating these two instruments has been used in previous studies [7,27], as it provides an opportunity to compare observations from both instruments, thereby enhancing understanding and increasing confidence in the results.

However, directly comparing ASI and GPS observations presents challenges due to the differences in measurement principles, and their distinct spatial and temporal perspectives. To bridge this gap, the ionospheric pierce points (IPPs) of the GPS signals, defined as the locations where the ionosphere intersects the line of sight of the signal between GPS satellite and ground-based receiver [28], were projected onto the ASI images. We designed this spatial projection technique to reveal a precise spatial context of exactly where and when each GPS signal traveled through the ASI's field of view. This is key to determining whether a GPS signal was affected by the bubble, rather than merely a temporal coincidence between the presence of bubbles and the enhanced ROTI values, thereby adding clarity and confidence to the analysis. Several works have studied the longitudinal distribution of plasma bubbles [29-31]. For instance, [30] analyzed total electron content (TEC) measurements from 67 International GNSS Service (IGS) stations distributed along the geomagnetic equator during solar cycle 23 and showed that EPB occurrence rates are higher in the South American and African sectors compared to other longitudes. While extensive progress has focused on plasma bubble activity in eastern South America (Brazil) using multiple observational techniques [32-35], considerably fewer studies have investigated the statistical characteristics of spread-F and plasma bubbles in western South America, particularly in Argentina, through GNSS and ionosonde measurements [36-39].

This study analyses the features of plasma bubbles on September 13, 2017, using data from El Leoncito ASI combined with data from the co-located GPS receiver over Argentina. The objective is to visually identify plasma bubbles via airglow emissions and investigate their intersection with GPS signals paths and correlate these intersections with ROTI values to understand how the bubbles distort these signals. For that purpose, the IPP locations were calculated and projected onto the ASI images, enabling direct spatial and temporal comparison between optical and radio-based observations.

2. Data & Instruments

In this work, the utilized airglow measurements were obtained from the El Leoncito ASI, which was installed by Boston University Imaging Science group at Complejo Astronomico El Leoncito (CASLEO) in Argentina (31.8^{o} S, 69.3^{o} W, 18.2^{o} S mag lat). Furthermore, the GPS observations–from the EL Leoncito GPS receiver station (31.8^{o} S, 69.293^{o} W), located approximately at the same location as the imager, were incorporated. Figure 1 illustrates the geographical locations of the two instruments, where the ASI is represented by the red circle and the receiver station by the black star.

Fig.1: The locations of El Leoncito ASI (red circle) and the GPS receiver station (black star). The dashed circle indicates the ASI's field of view.

Regarding the ASI, it is equipped with a wheel containing five wavelength filters (557.7 nm, 630.0 nm, 777.4 nm 589.3 nm, and > 695.0 nm) for detecting different phenomena at different altitudes, in addition to a background filter at 644.4 nm [40]. This study focuses on the wavelength of 630.0 nm, emitted from the de-excitation of 1D excited oxygen atoms that are produced through the dissociative recombination of O_2^+ [41,42]. The El Leoncito ASI detector consists of a 2046 × 2046-pixel bare charge coupled device (CCD) array. During data collection, the captured images are binned at a 3 × 3 resolution, resulting in 682 × 682- pixel images [43]. On September 13, 2017, observations started after local sunset at 18:23 (LT) and continued until just before local sunrise at 4:30 (LT). The image repetition rate for the used wavelength is approximately 9 minutes, resulting in a total of 66 images captured during the night.

The GPS data for this night were acquired from the Low Latitude Ionospheric Sensor Network (LISN). The GPS observations detected the plasma bubbles using the ROTI index, which was computed using MATLAB software (calcul_roti_v411.m), developed by R.Fleury. Slant Total Electron Content (STEC) was derived from phase measurements of GPS signals in RINEX 2.11 format, in units of TECU (1TECU = 10^{16} electrons/ m^2). The phase jumps were identified when consecutive 30-second data points exhibited a difference greater than 5 TECU; to detect and correct these non-physical jumps, a polynomial regression was applied to smooth the STEC data [44]. From the STEC temporal gradient at 30-second intervals, the Rate of TEC (ROT) was calculated in units of TECU /min. Then, the ROTI index was calculated as the standard deviation of the ROT values over 5 minutes [45]. In this study, to reduce multipath errors, ROTI was computed using GPS signals with elevation angles greater than 25°. Furthermore, the ROTI threshold value used to identify irregularities, established by comparing values observed during quiet ionospheric conditions, was set at 0.5 TECU /min.

3. Methodology for Mapping IPPs to ASI Image Coordinates

To facilitate an accurate comparison between the observations from the ASI and GPS, it is essential to examine the crossing of the received GPS signals paths through the airglow depletion. This can be achieved by projecting the IPPs onto the airglow images. The IPP represents the location where the GPS signal line of sight intersects the ionosphere, which is typically modeled as a thin shell [46]. This shell is located near the peak of the F layer [47], generally at an altitude between approximately 350 km and 500 km, where ionospheric irregularities are considered to have the most significant impact on the signal [48]. The geographic coordinates of the IPP are traditionally calculated using the method described by [49,50], which remains widely used in ionospheric studies due to its simplicity and efficiency. This approach determines the IPPs geographic latitude (ϕ_{ipp}) and longitude (λ_{ipp}) at a specified ionospheric altitude (h_{ipp}) using the receiver coordinates, along with the direction of the incoming signal, using the following equations:

$$\phi_{ipp} = \sin^{-1}[\sin(\phi_r)\cos(\psi) + cos(\phi_r)\sin(\psi)\cos(Az)]$$

$$\lambda_{ipp} = \lambda_r + sin^{-1}[\sin(\psi)]$$

With ψ represent the earth's centered angle between the receiver and IPP given by:

$$\psi = \frac{\pi}{2} - El - \sin^{-1}\left[\frac{R_e}{R_e + h_{ipp})}\cos(El)\right]$$

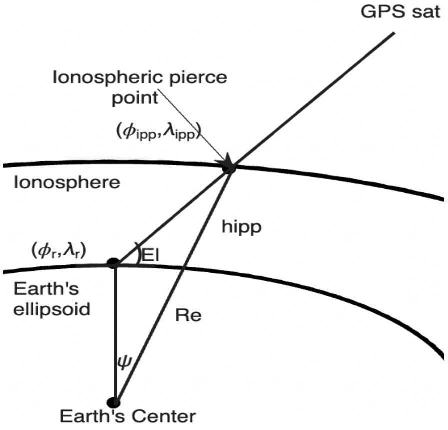

Fig.2: Geometry of ionospheric pierce point calculation, Adapted from [51], with modifications.

Where ϕ_r and λ_r are the geographic latitude and longitude of the receiver station, R_e = 6371 km is the mean Earth radius, h_{IPP} =450 km, *Az* and *El* are the azimuth and elevation angles of the GPS satellite, which define the signal direction relative to the receiver.

After calculating the geographic coordinates of the IPPs, they were converted into pixel coordinates to project them onto the ASI images. This conversion was achieved by comparing the imager's actual field of view (FOV) with the area representing the airglow data in the ASI images, to determine a scaling factor between geographic and pixel coordinates. The actual FOV of the imager depends on the emission height and its zenith angle, which is set at 80° for the El Leoncito ASI as described by [40]. Our study assumed the altitude of the airglow emission layer at 250 km, which corresponds to the expected emanation altitude of OI 630.0 nm emissions and is appropriate under conditions of low solar activity [40, 52]. Based on this altitude and the operating zenith angle, the FOV forms an area with a radius of 996 km, represented by the black dashed circle in Figure 1. On the other hand, a mask was applied to the ASI images to isolate the region associated with the airglow emissions. This region was manually defined based on the optical footprint of the imager, as a circular area with a radius of 262 pixels from the image center. The pixels outside this circle were set to white color, while preserving the original image dimensions. Figure 3 illustrates this process, with the original image shown on the left and the masked image on the right. This step ensured accurate identification of the spatial boundaries of the usable FOV for airglow observation, within which IPPs are expected to appear in the ASI images.

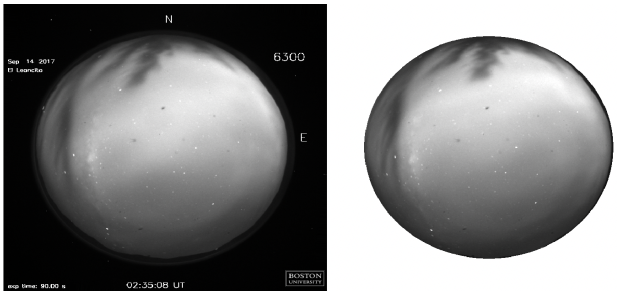

Fig.3: The original OI 630.0 nm image taken by All-Sky imager (on left), and the masked image (on right).

By comparing the physical radius of the imager's actual FOV with the pixel radius of the masked image, the scaling factor (SF) was 3.8 kilometers corresponding to 1 pixel. After computing the scaling factor and to finding the pixel latitude (ϕ_{pixel}) and longitude (λ_{pixel}) of the IPPs, the geographic latitude and longitude offsets between each IPP and the imager's location were calculated. These angular offsets were then converted to physical distances (in kilometers) using standard geodetic scaling: latitude differences were multiplied by 111.32 km per degree, while longitude differences were multiplied by the same factor adjusted by the cosine of latitude. Next, these distances were converted into pixel units using the predefined kilometer-to-pixel scaling factor. Finally, the pixel coordinates were referenced to the image center, where (341, 341) pixels corresponds to the imager's position in the image, by adding 341.

The pixel coordinates were given as:

$$\phi_{pixel} = [\left(\phi_{ASI} - \phi_{ipp}\right) * 111.32 * \frac{1}{SF} + 341$$

$$\lambda_{pixel} = \left(\lambda_{ipp} - \lambda_{ASI}\right) * 11.32 \cos(\phi_{ipp}) * \frac{1}{SF} + 341$$

Where ϕ_{ASI} and λ_{ASI} are the geographic latitude and longitude of the imager. Where ϕ_{r} and λ_{r} are the geographic latitude and longitude of the receiver station. the scaling factor (SF) was 3.8 kilometers.

4. Observations

4.1 ASI Observations

The ASI provides a spatiotemporal observation of the plasma bubbles, where they are identified as dark regions relative to the surrounding ionosphere [53], resulting from localized reductions in the 630.0 nm airglow emission intensity. This reductions in brightness corresponds to a depletion in electron density within the ionospheric F-region. To classify these features as plasma bubbles, several criteria must be met: (1) the depletion must persist for a minimum duration of one hour in sequential images; (2) the structures should appear elongated along the geomagnetic field lines in north–south direction; (3) they should exhibit temporal development, such as growth in size and/or intensity; and often typically drift eastward over time.

On the night of September 13, 2017, ASI observations were conducted from 18:23 LT to 04:30 LT. However, the clear airglow data were available only until 23:36 LT. The development, evolution, and decay of the plasma bubbles were observed between 19:52 LT and 23:36 LT. Figure 4 shows a series of ASI images illustrating approximately the complete life cycle of the detected plasma bubbles.

The initial detection of plasma bubble activity occurred around 19:52 LT, when two dark bands were observed in the west and middle of the north region of the FOV. At 20:20 LT, another dark band appeared from the west. These dark bands gradually became more defined, increased in size, and moved eastward over time, which is typical of the post-sunset plasma bubble dynamics. As they moved, the darkness of the bands initially intensified, peaking between 21:25 and 22:21 LT.

Between 21:35 and 23:18 LT, some of the existing bubbles began to branch, forming multiple distinct depletion structures. These structures were relatively narrow, elongated along the geomagnetic field lines, and exhibited consistent eastward motion.

By 22:49 LT, the bubble structures became fainter, and their contrast against the airglow background significantly decreased; however, they remained visible until around 23:36 LT. By that time, most of the depletion features had already faded, marking the end of the main event. Furthermore, the increased brightness that appeared in the northern portion compromised the reliability of the observations. Consequently, the data collected after 23:36 LT were deemed unsuitable for further analysis of plasma bubble activity.

4.2 ROTI Observations

The ROTI index was computed using GPS signals to investigate ionospheric irregularities during this night. The analysis focused on the period between 20:00 and 24:00 LT, chosen to align with the time window of plasma bubble observations for a direct comparison. Figure 5 illustrates a noticeable enhancement in the ROTI index recorded approximately between 21:00 and 22:00 LT.

The values began to increase gradually at 21:09 LT, reaching 1.23 TECU/min by 21:18 LT. After a slight decrease, the index dropped sharply to a normal level at 21:24 LT. Following this, the values surged again at 21:30 LT, peaking approximately at 21:37 LT with a maximum of 1.44 TECU/min, before declining gradually and returning below the threshold at 2:55 UT.

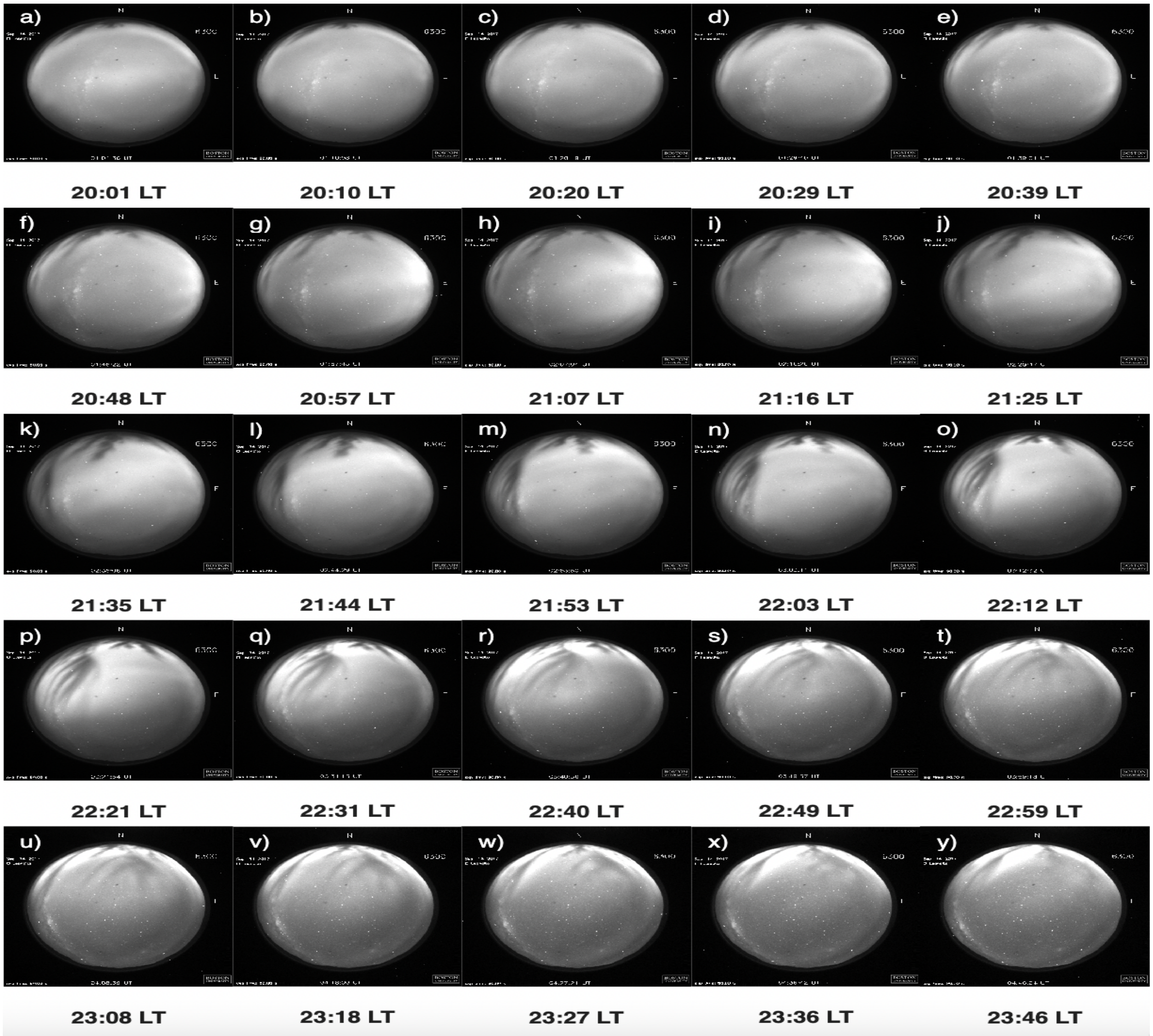

Fig. 4: A sequence of OI 630.0 nm images illustrates the evolution of plasma bubbles for the night of September 14, 2017.

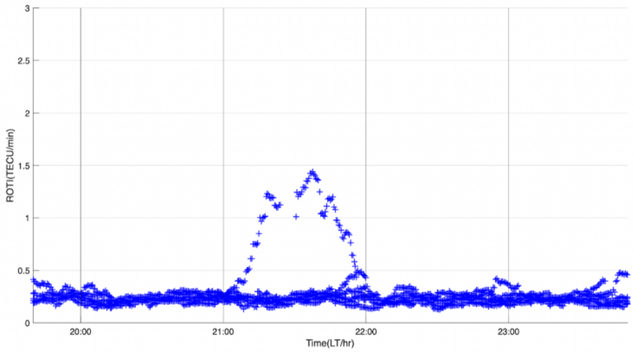

Fig. 5: GPS ROTI variations on the night of September 14, 2017, during the plasma bubbles observation period.

This elevated ROTI activity reflects the presence of significant ionospheric irregularities. In contrast, during the initial and final intervals of the selected period, the values remained consistently low, generally below 0.5 TECU/min.

4.3 Projection of IPPs onto ASI Images for Spatial Analysis.

The geographic coordinates of the IPPs were calculated for each signal using its direction relative to the receiver, along with the receiver coordinated and the assumed ionospheric shell height of 450 km. Then they were converted into pixel coordinates and mapped onto the ASI images, allowing for spatial comparison between the GPS signal paths and the observed plasma bubbles. One of the key challenges in this approach was the mismatch in temporal resolution between the ROTI data and the airglow images.

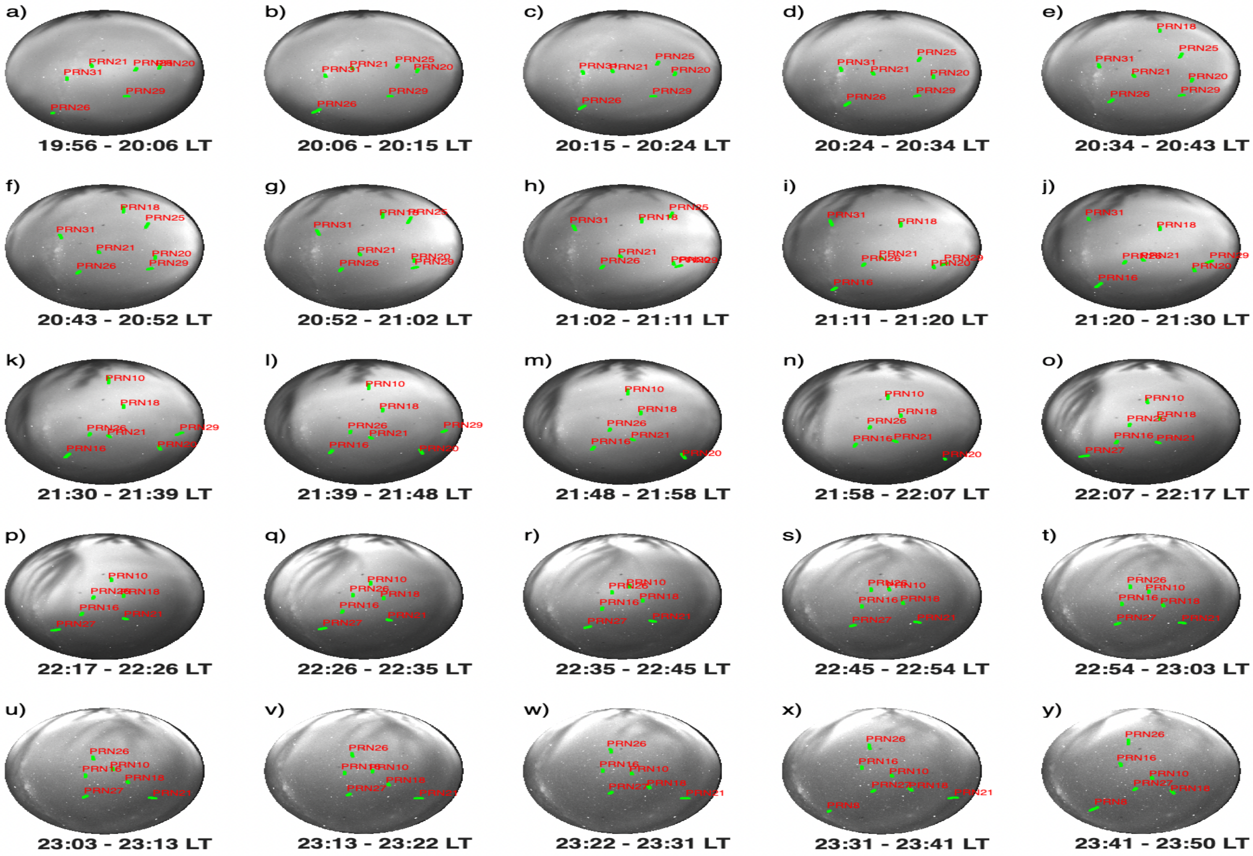

Fig. 6: The IPPs of GPS satellite signals (green points), corresponding to the image time and all 30-second steps within ±4.5 minutes, were projected on the airglow images.

While the ROTI values were computed at a 30-second cadence, the ASI captured the airglow images approximately every 9 minutes. To enable a meaningful spatial and temporal comparison, the IPPs were projected onto the images not only for the exact time of each airglow image, but also for each 30-second interval within a ±4.5-minute window around the image timestamp. This approach allowed multiple IPPs to be projected onto a single image, effectively compensating for the lower temporal resolution of the ASI data and capturing the signals trajectories that passed through or near the observed depletion regions during that period. Figure 6 displays a sequence of 25 airglow images with small green markers superimposed on each image to represent the projected IPPs points of different PRN signals (PRN: Pseudo-Random Noise code number used to identify individual GPS satellites).

A detailed visual inspection of the images in Figure 8 reveals several instances where the IPP traces of the signals intersect with plasma bubble structure. For instance, in image (i), the IPPs corresponding to PRN 31 passed through a well-defined bubble located in the northwest portion of the image. In the subsequent image, the IPP trace from the same PRN continued along a path that crosses a fainter region, suggesting a weaker depletion. Additionally, in image (k), the IPPs from PRN 10 passed through an area of active plasma bubble, located in the central-northern sector of the image, for a short period. Then the interaction became more significant in image (l), where the IPPs visibly overlapped a pronounced depletion band.

Focusing on this analysis, the timing of the images depicting the intersection of the plasma bubbles and the signal traces coincides with the time interval of elevated ROTI values. This suggests that the plasma bubbles are responsible for the ionospheric irregularities detected in the GPS data during this period. To validate this inference, the ROTI values associated with the GPS signals received within this timeframe were analyzed separately in the next section, with particular attention given to determining whether the elevated ROTI originated specifically from the signals whose paths intersected the plasma bubbles.

4.4 Correlation Between Plasma Bubbles, IPPs, and ROTI

For further investigation, Figure 7 presents the spatial relationship between signal paths and plasma bubble structures (upper panel), along with the corresponding ROTI variations (lower panel), for the period from 21:00 to 22:00 LT.

As illustrated in Figure 7g, PRN 31 exhibited a consistent increase in ROTI values from approximately 21:04 to 21:24 LT. A gradual rise began around 21:04 LT, but the values remained below 0.5 TECU, as the signal started approaching the plasma bubbles, as seen in figure 7a. By 21:11 LT, the ROTI values increased, coinciding with the intersection between the signal and the bubbles (figure 7b). Between 21:18 and 21:24 LT, the signal appeared to pass through a region with less depletion, which likely contributed to more rapid electron density fluctuations, further enhancing the ROTI that peaked at 1.2 TECU/min.

Furthermore, PRN 10 showed elevated ROTI values between 21:30 and 21:55 LT as illustrated in figure 7o. The values began at approximately 1 TECU/min when the signal briefly intersected the bubble region from the north at 21:30 LT, before moving into a regular ionospheric region as seen in figure 7d, resulting in an enhancement in ROTI due to the abrupt density gradient. After a slight drop, the ROTI rose followed by a gradual decline, falling below the threshold at 21:55 LT as the signal path returned to a more stable ionospheric environment (figure 7f). These findings support the earlier inference that plasma bubble structures were the again at 21:43 LT as the signal re-entered the depleted region (figure 7e), cause of the ionospheric irregularities detected in the ROTI data, as the signals crossed them. In addition, the novel finding from this case study is that ROTI values were elevated not only when the signal passed through the plasma bubbles, but also when it transitioned from a depleted region to a more uniform ionosphere. This consist with [47], which reported that scintillation is most pronounced along the steep walls of equatorial plasma bubbles in India (Kolhapur). The enhancement of ROTI, in turn, affects the performance of positioning systems, by degrading GPS signal quality, reducing the number of visible satellites, and increasing the occurrence of cycle slips, which ultimately elevates the errors of GPS Precise Point Positioning (PPP) solutions.

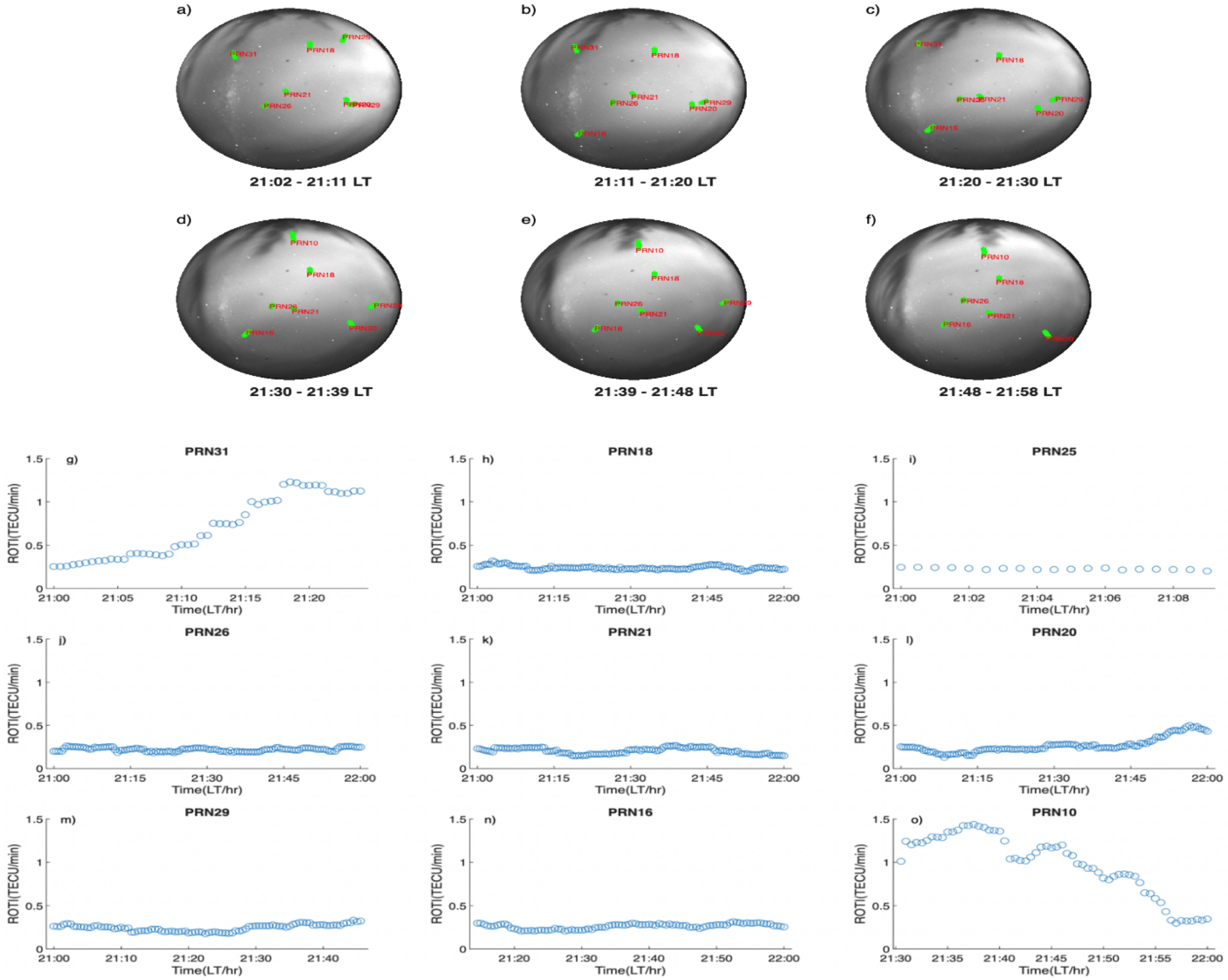

Fig. 7: The airglow images with projected IPPs illustrate the intersection of each satellite's signal path with plasma bubbles during the interval between 21:00 and 22:00 LT (upper panel). The corresponding ROTI variations of these satellites are shown individually during this period (lower panel).

This is consistent with the findings in [54], who demonstrated a strong positive correlation between ROTI and 3D root mean square (RMS) positioning errors, as well as with the percentage of errors exceeding 0.5 m.

In contrast, the other PRNs exhibit relatively flat ROTI profiles, with values generally remaining below 0.5 TECU/min throughout the observation period. These quiet signatures indicate that the corresponding signal paths did not intersect any ionospheric irregularities during this time window, which is consistent with the findings in the upper panel of Figure 7. It is worth noting that PRN 25 displays a very limited time series, with ROTI data only available between 21:00 and approximately 21:09 LT.

Conclusion

This study presented a comprehensive analysis of plasma bubbles by combining data from the El Leoncito all-sky imager and co-located GPS receiver during the night of September 13–14, 2017. The ASI images revealed the formation, evolution, and decay of several PBs. Concurrently, the ROTI index derived from GPS measurements indicated the presence of ionospheric irregularities precisely during the plasma bubbles period. Both datasets were used to compare the timing and location of airglow depletions with the GPS signal trajectory, by calculating the coordinates of the signals IPPs and projecting them onto ASI images. This approach was designed to evaluate whether the GPS signals traversed plasma bubbles and how this influenced the values of ROTI. This approach provides clear evidence that the PBs were responsible for the ionospheric disruptions causing the observed enhancement of ROTI. In particular, for satellites PRN 10 and PRN 31, ROTI noticeably increased when their signals traversed through the plasma bubbles, whereas the signals whose paths did not cross the bubbles exhibited minimal and stable ROTI variations, below the threshold. The most significant finding from this work is that, not just the crossing through the bubbles, but also the transitions between depleted and more uniform ionospheric regions can lead to significant increases in ROTI, likely due to steep electron density gradients. These findings enhance our understanding of EPB and the ionospheric irregularities it induces, as well as their impact on GPS signals.

Acknowledgments

The authors are grateful to the Low Latitude Ionospheric Sensor Network (LISN) project team for providing the GPS data required in this work.

References

[1] Tsunoda RT. Magnetic-field-aligned characteristics of plasma bubbles in the nighttime equatorial ionosphere. J Atmos Terr Phys. 1980;42:143-152. doi:10.1016/0021-9169(80)90057-4

[2] Kelley MC. The Earth's Ionosphere: Plasma Physics and Electrodynamics. Academic Press; 1989.

[3] Fejer BG, Scherliess L, de Paula ER. Effects of the vertical plasma drift velocity on the generation and evolution of equatorial spread F. J Geophys Res. 1999;104:19859-19869. doi:10.1029/1999JA900271

[4] Aa E, Zou S, Eastes R, et al. Coordinated ground-based and space-based observations of equatorial plasma bubbles. J Geophys Res Space Phys. 2020;125(1):e2019JA027569. doi:10.1029/2019JA027569

[5] Otsuka Y. Review of the generation mechanisms of post-midnight irregularities in the equatorial and low-latitude ionosphere. Prog Earth Planet Sci. 2018;5:57. doi:10.1186/s40645-018-0212-7

[6] Sultan PJ. Linear theory and modeling of the Rayleigh-Taylor instability leading to the occurrence of equatorial spread F. J Geophys Res. 1996;101:26875-26892. doi:10.1029/96JA00682

[7] Okoh D, Rabiu B, Shiokawa K, et al. First study on the occurrence frequency of equatorial plasma bubbles over West Africa using an all-sky airglow imager and GNSS receivers. J Geophys Res Space Phys. 2017;122:12430-12444. doi:10.1002/2017JA024602

[8] Kelley MC, Makela JJ, Paxton LJ, et al. The first coordinated ground- and space-based optical observations of equatorial plasma bubbles. Geophys Res Lett. 2003;30(14):1766. doi:10.1029/2003GL017301

[9] Nishioka M, Basu Su, Basu S, et al. C/NOFS satellite observations of equatorial ionospheric plasma structures supported by multiple ground-based diagnostics in October 2008. J Geophys Res. 2011;116:A10323. doi:10.1029/2011JA016446

[10] Abdu MA, de Medeiros RT, Sobral JHA, Bittencourt JA. Spread F plasma bubble vertical rise velocities determined from spaced ionosonde observations. J Geophys Res. 1983;88:9197-9204. doi:10.1029/JA088iA11p09197

[11] Abadi P, Otsuka Y, Supriadi S, Olla A. Probability of ionospheric plasma bubble occurrence as a function of pre-reversal enhancement deduced from ionosondes in Southeast Asia. AIP Conf Proc. 2020;2226:050001. doi:10.1063/5.0002321

[12] Otsuka Y, Abadi P, Hozumi K, Almahi A. Equinoctial asymmetry of plasma bubble occurrence and electric field at evening: GPS and ionosonde measurements in Southeast Asia. J Atmos Solar Terr Phys. 2023;252:106136. doi:10.1016/j.jastp.2023.106136

[13] Ajith KK, Tulasi Ram S, Yamamoto M, et al. Explicit characteristics of evolutionary-type plasma bubbles observed from Equatorial Atmosphere Radar during the low to moderate solar activity years 2010-2012. J Geophys Res Space Phys. 2015;120(2):1371-1382. doi:10.1002/2014JA020878

[14] Liu H, Doornbos E, Nakashima J. Thermospheric wind observed by GOCE: Wind jets and seasonal variations. J Geophys Res Space Phys. 2016;121:6901-6913. doi:10.1002/2016JA022938

[15] Tulasi Ram S, Ajith KK, Yokoyama T, et al. Vertical rise velocity of equatorial plasma bubbles estimated from Equatorial Atmosphere Radar (EAR) observations and HIRB model simulations. J Geophys Res Space Phys. 2017;122(6):6584-6594. doi:10.1002/2017JA024260

[16] Bumrungkit A, Supnithi P, Saito S, Myint LMM. A study of equatorial plasma bubble structure using VHF radar and GNSS scintillations over the low-latitude regions. GPS Solut. 2022;26:148. doi:10.1007/s10291-022-01321-4

[17] Jin Y, Xiong C, Clausen L, et al. Ionospheric plasma irregularities based on in situ measurements from the Swarm satellites. J Geophys Res Space Phys. 2020;125(7):e2020JA028103. doi:10.1029/2020JA028103

[18] Martinis C, Daniell R, Eastes R, et al. Longitudinal variation of postsunset plasma depletions from the global-scale observations of the limb and disk (GOLD) mission. J Geophys Res Space Phys. 2021;126(2):e2020JA028510. doi:10.1029/2020JA028510

[19] Zakharenkova I, Cherniak I, Braun JJ, Wu Q. Global maps of equatorial plasma bubbles depletions based on FORMOSAT-7/COSMIC-2 ion velocity meter plasma density observations. Space Weather. 2023;21:e2023SW003438. doi:10.1029/2023SW003438

[20] Sun L, Xu J, Wang W, et al. A statistical analysis of equatorial plasma bubble structures based on an all-sky airglow imager network in China. J Geophys Res Space Phys. 2016;121(11):11495-11517. doi:10.1002/2016JA022950

[21] Gurav O, Ghodpage R, Patil P, et al. Occurrence climatology of equatorial plasma bubbles (EPBs) using optical observations over Kolhapur, India during solar cycle-24. Ann Geophys. 2020;63(6):CL664. doi:10.4401/ag-8068

[22] Saha S, Pallamraju D, Ghodpage RN. Investigations of equatorial plasma bubbles as observed in the OI 630 nm nightglow emissions over off-equatorial and low-latitudinal locations over Indian longitudes. Adv Space Res. 2022;70(11):3686-3698. doi:10.1016/j.asr.2022.08.023

[23] Ma X, Wu M, Guo P, Xu J. Airglow observation and statistical analysis of plasma bubbles over China. Atmosphere. 2023;14(2):341. doi:10.3390/atmos14020341

[24] Seif A, Abdullah M, Hasbi AM, Zou Y. Investigation of ionospheric scintillation at UKM station, Malaysia during low solar activity. Acta Astronaut. 2012;81:92-101. doi:10.1016/j.actaastro.2012.06.024

[25] Sori T, Shinbori A, Otsuka Y, Tsugawa T, Nishioka M. The occurrence feature of plasma bubbles in the equatorial to midlatitude ionosphere during geomagnetic storms using long-term GNSS-TEC data. J Geophys Res Space Phys. 2021;126:e2020JA029010. doi:10.1029/2020JA029010

[26] Carmo CS, Dai L, Denardini CM, et al. Equatorial plasma bubbles features over the Brazilian sector according to the solar cycle and geomagnetic activity level. Front Astron Space Sci. 2023;10:1252511. doi:10.3389/fspas.2023.1252511

[27] Nade DP, Shetti DJ, Sharma AK, et al. Geographical analysis of equatorial plasma bubbles by GPS and nightglow measurements. Adv Space Res. 2015;56(9):1901-1910. doi:10.1016/j.asr.2015.03.030

[28] Seeber G. Satellite Geodesy. Berlin: Walter de Gruyter; 2003.

[29] Aa E, Zou S, Liu S. Statistical analysis of equatorial plasma irregularities retrieved from Swarm 2013–2019 observations. J Geophys Res Space Phys. 2020;125(4):e2019JA027022. doi:10.1029/2019JA027022

[30] Magdaleno S, Herraiz M, Altadill D, de la Morena BA. Climatology characterization of equatorial plasma bubbles using GPS data. J Space Weather Space Clim. 2017;7:A3. doi:10.1051/swsc/2016039

[31] Nishioka M, Saito A, Tsugawa T. Occurrence characteristics of plasma bubble derived from global ground-based GPS receiver networks. J Geophys Res. 2008;113:A05301. doi:10.1029/2007JA012605

[32] Yeboah EA, Fagundes PR, Tardelli A, Pillat VG, Pignalberi A, Kavutarapu V, et al. Ground and satellite-based observations of ionospheric plasma bubbles and blobs at 5.65° latitude in the Brazilian sector. Adv Space Res. 2021;67:2416–2438. doi:10.1016/j.asr.2021.01.034

[33] Sobral JHA, Abdu MA, Takahashi H, Taylor MJ, De Paula ER, Zamlutti CJ, et al. Ionospheric plasma bubble climatology over Brazil based on 22 years (1977–1998) of 630 nm airglow observations. J Atmos Sol-Terr Phys. 2002;64:1517–1524. doi:10.1016/S1364-6826(02)00089-5

[34] Haase JS, Dautermann T, Taylor MJ, Chapagain N, Calais E, Pautet D. Propagation of plasma bubbles observed in Brazil from GPS and airglow data. Adv Space Res. 2011;47(10):1758–1776. doi:10.1016/j.asr.2010.09.025

[35] Sahai Y, Fagundes PR, Bittencourt JA. Transequatorial F-region ionospheric plasma bubbles: solar cycle effects. J Atmos Sol-Terr Phys. 2000;62:1377–1383. doi:10.1016/S1364-6826(00)00179-6

[36] Gonzalez G. Spread-F characteristics over Tucumán near the southern anomaly crest in South America during the descending phase of solar cycle 24. Adv Space Res. 2022;69(3):1281–1300. doi:10.1016/j.asr.2021.11.009

[37] Pietrella M, Pezzopane M, Fagundes PR, de Jesus R, Supnithi P, Klinngam S, et al. Equinoctial spread-F occurrence at low latitudes in different longitude sectors under moderate and high solar activity. J Atmos Sol-Terr Phys. 2017;164:149–162. doi:10.1016/j.jastp.2017.07.007

[38] Alfonsi L, Spogli L, Pezzopane M, Romano V, Zuccheretti E, De Franceschi G, et al. Comparative analysis of spread-F signature and GPS scintillation occurrences at Tucumán, Argentina. J Geophys Res Space Phys. 2013;118:4483–4502. doi:10.1002/jgra.50378

[39] Pezzopane M, Zuccheretti E, Abadi P, de Abreu AJ, de Jesus R, Fagundes PR, et al. Low-latitude equinoctial spread-F occurrence at different longitude sectors under low solar activity. Ann Geophys. 2013;31:153–162. doi:10.5194/angeo-31-153-2013

[40] Martinis C, Wilson J, Zablowski P, et al. A new method to estimate cloud cover fraction over El Leoncito Observatory from an all-sky imager designed for upper atmosphere studies. Publ Astron Soc Pac. 2013;125(923):56-67. doi:10.1086/669255

[41] Sahai Y, Abalde JR, Fagundes PR, Pillat VG, Bittencourt JA. First observations of detached equatorial ionospheric plasma depletions using OI 630.0 nm and OI 777.4 nm emissions nightglow imaging. Geophys Res Lett. 2006;33:L11104. doi:10.1029/2005GL025262

[42] Martinis C, Baumgardner J, Wroten J, Mendillo M. All-sky imaging capabilities for ionospheric space weather research using geomagnetic conjugate point observing sites. Adv Space Res. 2018;61:1636-1651. doi:10.1016/j.asr.2017.07.021

[43] Martinis C, Yokoyama T, Nishioka M. All-sky imaging observations and modeling of bright 630-nm airglow structures associated with MSTIDs. J Geophys Res Space Phys. 2019;124:7332-7340. doi:10.1029/2019JA026935

[44] Alenazi MS, Nooreldeen HM, Ahmed AM, et al. Investigation of ionospheric response to a moderate geomagnetic storm over the mid-latitude of Saudi Arabia. Open Astron. 2025;34(1):20240009. doi:10.1515/astro-2024-0009

[45] Pi X, Mannucci AJ, Lindqwister UJ, Ho CM. Monitoring of global ionospheric irregularities using the Worldwide GPS Network. Geophys Res Lett. 1997;24:2283-2286. doi:10.1029/97GL02273

[46] Bang E, Lee J. Methodology of automated ionosphere front velocity estimation for ground-based augmentation of GNSS. Radio Sci. 2013;48:659-670. doi:10.1002/rds.20066

[47] Sharma AK, Gurav OB, Gaikwad HP, et al. Study of equatorial plasma bubbles using all sky imager and scintillation technique from Kolhapur station: a case study. Astrophys Space Sci. 2018;363:83. doi:10.1007/s10509-018-3303-4

[48] Hoque MM, Jakowski N, Prol FS. A new climatological electron density model for supporting space weather services. J Space Weather Space Clim. 2022;12:1. doi:10.1051/swsc/2021044

[49] Matsuoka MT, Camargo PDO. Cálculo do TEC usando dados de receptores GPS de dupla frequência para a produção de mapas da ionosfera para a região brasileira. Rev Bras Cartogr. 2004;56(1):14-27.

[50] Prol FS, Camargo PO. Review of tomographic reconstruction methods of the ionosphere using GNSS. Rev Bras Geofís. 2015;33(3).

[51] Ya'acob N, Abdullah M, Ismail M. Determination of GPS total electron content using single layer model (SLM) ionospheric mapping function. Int J Comput Sci Netw Secur. 2008;8.

[52] Saha S, Pallamraju D. Latitudinal variations in the nocturnal behaviour of OI 630 nm airglow emissions and their relationship with the equatorial electrodynamics. J Atmos Sol-Terr Phys. 2022;241:105965. doi:10.1016/j.jastp.2022.105965

[53] Hickey DA, Martinis CR, Mendillo M, et al. Simultaneous 6300 Å airglow and radar observations of ionospheric irregularities and dynamics at the geomagnetic equator. Ann Geophys. 2018;36:473-487. doi:10.5194/angeo-36-473-2018

[54] Zhang Z, Wang N, Liu A, Li Z, Li A, Wang L, Zhang Y. Assessing 1-second ROTI for ionospheric perturbation monitoring using real-time multi-GNSS data in China. Space Weather. 2025;23:e2024SW004187. doi:10.1029/2024SW004187